Measurement and modeling of $Ar/H_2/CH_4$ arc jet discharge chemical vapor deposition reactors. I. Intercomparison of derived spatial variations of H atom, C_2, and CH radical densities

C. J. Rennick, J. Ma, J. J. Henney, J. B. Wills, M. N. R. Ashfold, and A. J. Orr-Ewing[a]
School of Chemistry, University of Bristol, Cantock's Close, Bristol BS8 1TS, United Kingdom

Yu. A. Mankelevich
Nuclear Physics Institute, Moscow State University, 119992 Moscow, Russia

Comparisons are drawn between spatially resolved absorption spectroscopy data obtained for a 6.4 kW dc arc jet reactor, operating with $Ar/H_2/CH_4$ gas mixtures, used for deposition of thin, polycrystalline diamond films, and the results of a two-dimensional (r,z) computer model incorporating gas activation, expansion into the low pressure reactor, and the chemistry of the neutral and charged species. The experimental measurements, using either cavity ring-down spectroscopy or diode laser absorption spectroscopy, determined absolute number densities of $H(n=2)$ atoms, and column densities of $C_2(a\,^3\Pi_u)$, $C_2(X\,^1\Sigma_g^+)$, and $CH(X\,^2\Pi)$ radicals, with vibrational and rotational quantum state resolutions, and their variation with height through the horizontally propagating arc jet plume. Spectra were also analyzed to obtain temperatures and local electron densities [from Stark broadening of $H(n=2)$ absorption lines]. The experimental data are directly compared with the output data of the model that returns spatially inhomogeneous temperature, flow velocities, and number densities of 25 neutral and 14 charged species. Under the base operating conditions of the reactor [11.4 SLM (standard liters per minute) of Ar and 1.8 SLM of H_2 entering the primary torch, with addition of 80 SCCM (SCCM denotes cubic centimeter per minute at STP) of CH_4 downstream; 6.4 kW input power; reactor pressure of 50 Torr], the calculated and measured column and number densities agree to within factors of 2–3, the model reproduces the spatial dependence of column densities, and the mean temperatures of $C_2(a)$ and $CH(X)$ radicals derived from spectra and model results are in good agreement. The model also captures the variation of these parameters with changes to operating conditions of the reactor such as flows of H_2 and CH_4, and input power. Further details of the model and the insights it provides are the subject of the accompanying paper [Mankelevich *et al.*, J. Appl. Phys. **102**, 063310 (2007)]. © *2007 American Institute of Physics*. [DOI: 10.1063/1.2783890]

I. INTRODUCTION

Thin films of poly-, nano-, and ultrananocrystalline diamond, diamondlike carbon (DLC), and carbon nanotubes (CNTs), grown by chemical vapor deposition (CVD) from a carbon-containing activated gas mixture, are increasingly finding important technological applications that include incorporation in low-field electron emission devices and chemical sensors.[1–3] The types of films grown and their rates of deposition depend on the substrate composition and temperature, the mixing ratios of feedstock gases such as CH_4, H_2, and Ar employed in the CVD reactor, and the method of activation of the mixture (e.g., microwave, radio frequency or dc arc discharge, or hot filament). Film compositions and morphologies are distinguished by, for example, the extent of sp^2 or sp^3 hybridization of the carbon atoms (evident from ratios of characteristic peaks in Raman spectra) and the sizes of crystalline domains.

dc arc jets offer considerable advantages as a route to deposition of polycrystalline diamond films at high growth

rates (up to $\sim 100\ \mu m/h$) when compared to alternative activation methods, but film quality is generally less spatially homogeneous than for deposition in an optimized microwave reactor. Jeffries and co-workers reported calibrated laser-induced fluorescence (LIF) measurements of the density distributions and temperatures of $C_2(a\,^3\Pi_u)$, $CH(X\,^2\Pi)$, and $C_3(X\,^1\Sigma_g^+)$ radicals in a 1.6 kW arc jet reactor plume (henceforth denoted as the SRI reactor)[4–6] and demonstrated that the $C_2(a)$ and $CH(X)$ densities peaked at the core of the plume, whereas the $C_3(X)$ densities maximized off axis in a cylindrical shell. A cascaded arc reactor used for deposition of amorphous diamond films has been extensively studied by Schram and co-workers using optical and other techniques.[7–14] Complementary computer modeling is essential to provide an understanding of the activation of a feedstock gas mixture, its expansion within an arc jet reactor, the chemistry in the resultant plume, and the deposition of material at a substrate.[5,15,16] In a series of recent studies,[17–23] we have developed laser-based absorption techniques to probe the highly activated environment of a 6.4 kW dc arc jet reactor plume, operating at a pressure of 50 Torr and capable of diamond film growth at rates up to 100 $\mu m/h$. The arc jet

---

[a])Author to whom correspondence should be addressed. FAX: +44 117 925 0612. Electronic mail: a.orr-ewing@bris.ac.uk
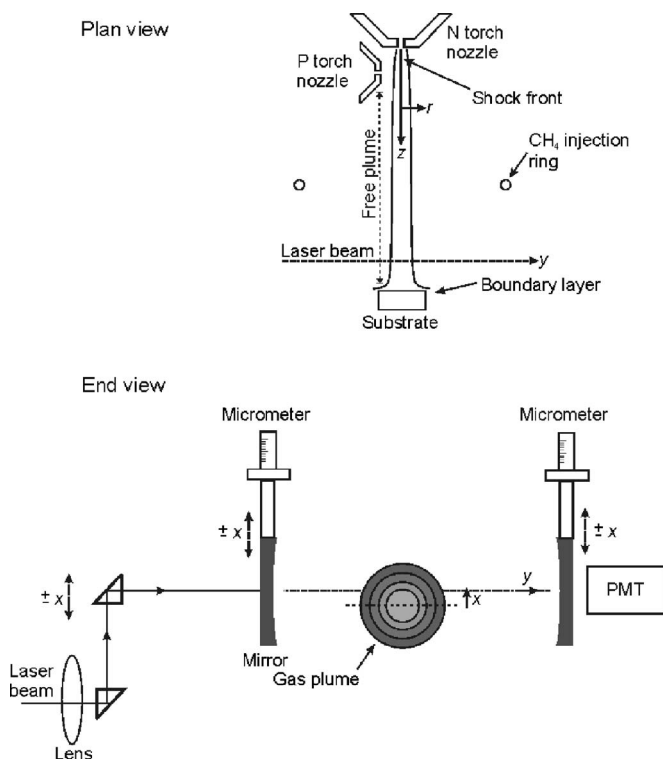
FIG. 1. Schematic plan and end-view diagrams of the arc jet reactor and plume. The x, y, z, and r coordinates used throughout are defined in the diagram. The end view shows the configuration of the laser beam and cavity mirrors used for spatially resolved CRDS measurements, with the arc jet plume propagating in a direction perpendicular to the plane of the diagram. Diode laser absorption measurements of the reactor used the setup illustrated in Ref. 23.

plume is shown schematically in Fig. 1, which identifies the key regions discussed further below and defines the Cartesian x,y,z and radial (r) coordinate systems used throughout the paper. Computational modeling studies, quantitative intercomparisons with experimental data, and thus rigorous tests of the model have resulted in a detailed understanding of the gaseous environment from the torch heads through to the substrate on which CVD takes place. We previously reported cavity ring-down spectroscopy (CRDS) absorption determinations of absolute column densities (number densities integrated along the line of sight of the laser beam used for absorption measurements) of $C_2(a\ ^3\Pi_u)$,[17,21] $C_2(X\ ^1\Sigma_g^+)$,[20] and $CH(X\ ^2\Pi)$ (Refs. 17 and 21) radicals in the arc jet plume operating on an $Ar/H_2/CH_4$ feed gas mixture and used rotationally resolved spectra and Doppler broadening of individual lines to estimate local gas temperatures. The outcomes, and their dependence on operating parameters of the dc arc jet reactor, were compared with preliminary model calculations.[18,21] For input flows of 1.8 SLM (standard liters per minute) of H_2 (F_{H_2}), 60 SCCM (SCCM denotes cubic centimeter per minute at STP) of CH_4 (F_{CH_4}), and an excess of argon (denoted by a flow F_{Ar}), to make up a total flow of 13.2 SLM, the CRDS measurements demonstrated mean C_2 temperatures of 3300 ± 200 K and respective column densities for $C_2(a)$ of $(1.1\pm0.4)\times10^{13}$ molecule cm^{-2}, $C_2(X)$ of $(3.0\pm0.9)\times10^{12}$ cm^{-2}, and $CH(X)$ of $(7.0\pm1.3)\times10^{12}$ molecule cm^{-2} when probing through the center of the plume in the free plume region. The

$C_2(a)$ and $CH(X)$ column densities increased markedly within a 5 mm boundary region in front of the substrate. Optical emission spectroscopy (OES) provided limited information on the spatial distributions of electronically excited C_2 molecules and H atoms in the plume, but was inadequate for characterizing the spatial inhomogeneity of the majority species populating ground and low-lying electronic states.

Initial attempts at producing a computer model of the chemistry prevailing in the Bristol arc jet reactor incorporated a limited chemical mechanism, with associated kinetics and thermochemistry, focusing solely on neutral species and chemistry. The model contained only a reduced dimensionality (previously referred to as "quasi-one-dimensional (1D)") treatment of the gas dynamics of the plume.[18] In this first generation of the simulations, species densities were computed as a function of z, the distance from the nozzle, but important two-dimensional effects such as radial diffusion and recirculation were accommodated by use of selected fitting parameters. Nevertheless, this relatively primitive model captured several features of the experimental measurements, such as the variation of radical densities with methane flow rate.

Rennick *et al.*[21] described comparisons of CRDS data with a more sophisticated model, in which chemical transformations, heat, and mass transfer were treated with full two-dimensional (r,z) cylindrical symmetry. The chemical mechanism involved 23 species and 76 reversible reactions, with temperature-dependent rate coefficients, but again neglected charged species except for Ar^+, ArH^+, and free electrons. Reaction of Ar^+ with H_2 to form ArH^+ and dissociative recombination with an electron is an important mechanism for dissociation of H_2 to H atoms and was thus incorporated. The calculations were performed for a reactor volume smaller than that of the arc jet apparatus to reduce the computational expense, and used estimates of the pressure, temperature, and degree of dissociation of H_2 (essentially complete) and degree of ionization of Ar (10%) in the gas flow at the nozzle orifice. The calculations produced r- and z-dependent distributions of key chemical species such as CH_x ($x=0-4$), C_2, C_2H, C_2H_2, and C_3 [with a mechanism that included C_2H_x ($x=0-6$), C_3H_x ($x=0-2$), C_4H_x ($x=0-2$)] and gave near-quantitative agreement with z-dependent measurements of C_2 and CH column densities. All experimental measurements were, however, summed along the line of sight of the laser beam, with measurements perpendicular to the center axis of the plume, and thus were largely insensitive to the radial variations of C_2 and CH predicted by the model: CH was calculated to peak in number density at the central axis of the plume ($r=0$), but C_2 showed an annular number density distribution, maximizing at $r=3$ mm. Radial diffusion of hydrocarbons and H_2 from the periphery of the plume, and subsequent reaction with activated species encountered in the core of the gas jet, is calculated to lead to such annular distributions for these and other radicals and atoms [excluding CH, C, and H($n=1$)], reminiscent of the annular distribution reported by Jeffries and co-workers[4–6] for spatially resolved LIF measurements of C_3 densities in the lower power SRI arc jet reactor. Results of these LIF measurements and calculations for both the Bristol

reactor and that studied by Jeffries and co-workers highlighted the importance of gas-flow recirculation in transporting carbon-containing species into the hot plume.

The chemical model employed to describe the C/H chemistry in the Bristol arc jet plume in the presence of added CH_4 is complicated, and is described in detail in the accompanying paper[24] and its associated electronic supplementary information. The starting conditions for the chemistry, as established by the temperature, energy content, degree of ionization, and chemical composition of the gas mixture expanding from the nozzle orifice and derived from an Ar/H_2 feedstock, must be well characterized for a correct treatment of all the subsequent chemistry. A necessary part of the evolution of the model was thus to step back and carry out extensive experimental and computational studies of the "base" plasma formed from the Ar/H_2 feedstock gas mixture in the absence of any added CH_4. Two preceding papers[22,23] described in detail the measurements and the first-principles modeling that were carried out on the Ar/H_2 plasma and demonstrate the significance of chemistry of charged species such as Ar^+, ArH^+, and electrons in the free plume region, particularly at low added flows of H_2. CRDS and spatially resolved diode laser absorption measurements of $H(n=2)$ column and number densities, obtained at Balmer-β (λ =486.1 nm) and Balmer-α (λ=656.3 nm) wavelengths, together with local electron densities, derived from Stark broadening of the H-atom absorption lines, were compared with model predictions and found to be in good accord. The electronically excited H atoms in this environment are formed by reaction of Ar^+ with H_2 to make the molecular ion ArH^+, followed by dissociative electron-ion recombination $[ArH^+ + e^- \rightarrow Ar + H(n)]$. Model predictions of the annular structure of the $H(n)$ atoms, supported by OES measurements of $H(n>2)$ atom emission and verified by spatially dependent absorption measurements,[23] are a consequence of diffusion of H_2 into the plume from its periphery, and reaction first with Ar^+ and then electrons, the number densities of which both peak at the core of the plume. The model also correctly described depletion of Ar^+ and retraction of the luminous plume as the input flow of H_2 increases, demonstrating the decreasing significance of chemistry involving charged species in the free plume region at the higher H_2 flows used for diamond growth in the reactor.

In the accompanying paper,[24] we build on the developments incorporated in the most recent model of the Ar/H_2 plasma system.[22] This model contained only the limited chemistry necessary to describe neutral and charged Ar/H species, with a total of 20 reversible processes including reactions, ionization, electron-ion recombination, relaxation (radiative and nonradiative) of excited state atoms, electron-impact excitation and quenching, and radiation trapping. This latter process must be incorporated because of the high number densities of ground state Ar and H atoms within the plume. We now include an extensive treatment of the additional H/C/Ar chemistry introduced by methane addition to the plume. Importantly, the model uses the initial conditions of temperature, pressure, flow velocity, degree of H_2 dissociation, and charged particle (Ar^+, H^+, ArH^+, e^-) densities

that were firmly established by the measurements and modeling for the base plasma (but with a further-refined estimation of H^+ contributions).

The details of the model are presented separately, but the current paper compares its outcomes with experimental measurements of the spatial variation of $C_2(a)$ and $CH(X)$ number densities and the effects of CH_4 addition on $H(n=2)$ and electron number densities, as well as our extensive body of prior measurements of the dependence of C_2 and CH abundances on arc jet operating conditions.[17,18,20,21] The significance of H_2 flow is addressed for the z dependence of the balance of ionic and neutral chemistries in the plume. The good agreement between experiment and theory demonstrates a satisfactory treatment of most of the plasma-chemical and gas-phase facets of the arc jet reactor, as used for CVD of diamond films. Using the radial variations of number densities of several radical species in proximity to the substrate, we can model the relative importance of these compounds on the growth of polycrystalline diamond films.

This paper is structured as follows. Section II contains a brief description of the arc jet and CRDS apparatus used for experimental measurements; detailed outcomes of the measurements and the model are compared in Sec. III, serving to validate the computational results, and discussed in the context of the mechanisms for formation of various radicals in the plume. A full description of the model is deferred to the companion paper,[24] where, to demonstrate its versatility, calculated results for the SRI arc jet reactor are also presented and compared with published experimental data.[4–6]

II. EXPERIMENTAL

A detailed description of the arc jet and the optical systems used for CRDS and diode laser absorption measurements has been given elsewhere,[17,20,22,23] and only a short summary of the key features is presented here. The adaptation of the CRD spectrometer to enable spatially resolved column density measurements of C_2 and CH is a recent modification, and hence is described thoroughly below. In the description that follows of the arc jet plume and the laser beams used to probe it, we adopt a coordinate system in which the plume propagates horizontally along z, with $z=0$ taken to be the main nozzle orifice, the laser beams propagate orthogonal to the plume along the y axis, (with z and y defining the horizontal plane), and the vertical coordinate used for spatial profiling is denoted as x (with $x=0$ corresponding to the center of the gas plume). It will also prove convenient to describe the properties of the cylindrically symmetric gas plume using the two-dimensional coordinates r and z, where r is a radial distance from the z axis in the xy plane.

The arc jet reactor (Aeroplasma Corp.) consists of two torch heads, denoted as the N and P torches, mounted at 90° to one another, with nozzles that inject an activated gas flow into a cylindrical vacuum chamber equipped with a variety of view ports and flanges for pumping lines and pressure gauges. The reactor is designed to work at input powers of up to 10 kW, but is typically operated at ~6.4 kW (80 A and 80 V). The N torch is mounted axially within the chamber,

usually operates with gas flows of 11.4 SLM of argon and 1.8 SLM of H_2 (backing pressures are 3–4 bars) and is the principal gas source for the plasma jet. The P torch contributes a further 0.75 SLM flow of a H_2/Ar mixture (approximately 1.3:1 H_2:Ar ratio) to stabilize the plasma, and 80 SCCM of methane is added 100 mm downstream of the N-torch nozzle orifice from an injection ring mounted concentrically with the activated Ar/H_2 plume. The average pressure in the reactor is maintained at 50 Torr. These power and gas-flow conditions of operation of the reactor will be referred to henceforth as standard conditions, and any deviations from them will be explicitly specified in the appropriate context.

Reference 22 contains a detailed diagram of the construction of the torch heads. The N torch has a double-chamber design, with the dc arc struck in the first chamber through an Ar flow of 10 SLM between a tungsten electrode and the copper torch body. Further flows of 1.4 SLM of Ar and 1.8 SLM of H_2 mix with this activated Ar plasma in the secondary stage of the torch, and the mixture expands through a 3.8 mm diameter orifice into the main reactor chamber. Modeling of the activation of the Ar/H_2 mixture, the almost complete dissociation of H_2, the degree of ionization of the argon, and the supersonic expansion through the torch nozzle to form the gas plume was discussed at length in Ref. 22.

Chemical vapor deposition occurs on a 26 mm diameter polished molybdenum substrate located typically at $z \geqslant 155$ mm from the nozzle orifice, and which can be translated along the z axis. The torches, substrate holder, and hollow-walled stainless steel chamber are cooled by a 9 bar flow of chilled water.

Two side arms fitted with 50 mm diameter quartz windows provide horizontal optical access for laser beam absorption measurements at the height of the gas plume. External cavity diode laser (ECDL) (Newport, $\lambda \sim 656$ nm) absorption measurements of H($n=2$) atom column densities are made with x resolution at $z=140$ mm by translating the height of the horizontally propagating laser beam using a two-prism periscope, as described in detail elsewhere,[23] with matching vertical motion of the photodiode detector located after the exit window. The ~ 1 MHz bandwidth laser is scanned rapidly and repeatedly across a 50 GHz portion of the H-atom Balmer-α absorption line, and comparison of input and transmitted intensities used to derive column densities from Beer-Lambert law analysis.

For CRDS experiments at a fixed height, $x=0$, the quartz windows are replaced with extension arms that terminate with finely adjustable mounts to hold the high-reflectivity cavity end mirrors ($R > 0.999$, planoconcave with 1 m radius of curvature). The tunable visible light from a Nd:YAG (yttrium aluminum garnet) pumped dye laser (Continuum Surelite III and Spectra Physics PDL-3 for C_2, CH, and H Balmer-β measurements) is injected along the y axis at $x =0$ and $z=145$ mm, and transmitted light intensities are monitored behind the exit mirror using a photomultiplier tube. The dye laser bandwidth of ~ 0.1 cm^{-1} must be taken into consideration when analyzing Doppler or Stark broadening of spectral lines. For CRDS measurements, the ring-down cavity (RDC) length is chosen to be 1 m, giving a near-confocal geometry, and a beam waist at the center of the cavity of 0.3 mm (defined as the radius at which the intensity of a Gaussian beam drops to $1/e^2$ of its maximum[25]). Beam shaping optics, incorporating a spatial filter and a lens mounted before the RDC, and careful optical alignment ensure excitation primarily of TEM$_{00}$ cavity modes.

Spatially resolved measurements of column densities at different heights x through the plume are achieved by simultaneous vertical translation of the RDC end mirrors and the input laser beam, while retaining optimum optical alignment. Figure 1 includes a schematic diagram of the apparatus employed. For these measurements, the cavity end mirrors were located within the vacuum chamber on adjustable mounts attached to linear feedthroughs fitted with micrometer threads. The laser beam was raised to the height of the center axis of the RDC using a periscope built from two right-angled prisms, with the upper prism mounted on a vertical translation stage. With careful alignment, the mirrors and periscope prism could be moved vertically by ±10 mm about $x=0$ without degradation of the cavity ring-down decays or of the TEM$_{00}$ mode coupling. Vertical profiling of the arc jet plume was thus possible with ~ 0.6 mm resolution, as determined by twice the laser beam waist. At each height, spectra of regions of the C_2 d $^3\Pi_g$-a $^3\Pi_u$ Swan band or CH A $^2\Delta$-X $^2\Pi$ band were recorded that spanned three resolved rotational lines, and the values of x were stepped first upwards then downwards (or vice versa) with random interleaving of heights to minimize the effects on spatial profiles of drift in the arc jet performance.

CRDS measurements were also made of the dependence of C_2 and CH column densities on proximity to the substrate by fixing the probe laser distance at $z=145$ mm from the N-torch nozzle and varying the z position of the substrate with submillimeter precision. These measurements were all made at a fixed height $x=0$ mm corresponding to the center of the plume.

All data collection and analysis used custom-written LABVIEW programs, operating either on an 8 bit digital oscilloscope (LeCroy WaveSurfer) or a personal computer (PC) communicating with an oscilloscope (Le Croy 9361) with a General Purpose Interface Bus (GPIB) interface. Frequency dispersion of all spectra was calibrated using a combination of a wavemeter and Fabry-Pérot etalons of known free spectral range. Molecular spectra were assigned using simulations generated from known spectroscopic constants[26,27] using the PGOPHER program.[28]

III. RESULTS OF THE EXPERIMENTAL MEASUREMENTS AND COMPARISON WITH MODEL OUTCOMES

The variations of the column densities of the C_2 radical, in both the ground (X $^1\Sigma^+_g$) and first excited (a $^3\Pi_u$) states, of CH(X) radicals and of H($n=2$) atoms have been measured in the arc jet reactor as a function of various operating parameters. Additionally, to obtain information on the radial profiles of $C_2(a)$, CH(X), and H($n=2$), column density measurements were made as a function of vertical position across the plasma plume. The experimental results presented in this

section are subdivided into those obtained from CRDS and diode laser absorption measurements of H($n=2$) atoms and data derived from CRDS measurements of carbon-containing radicals (C_2 and CH). The former results include information deduced about electron densities in the plasma from Stark broadening of hydrogen atom absorption lines. Throughout the section, experimental results will be compared quantitatively with the outcomes of the computer model described in the accompanying paper.[24]

For H($n=2$) atoms, column densities can be deduced from the experimental measurements without need for knowledge of the local gas temperature. For analysis of absorption spectrum data for C_2 and CH radicals, which span only a few rotational lines in a narrow wavenumber interval, deduction of total $C_2(a)$, $C_2(X)$, or CH(X) column densities or even column densities for these radicals in their ground vibrational levels [denoted as $C_2(a,v=0)$, $C_2(X,v=0)$, and CH($X,v=0$)] is not straightforward unless the temperature along the line of sight of the laser beam is uniform and known. This complication arises from the requirement that the conversion factor be calculated to obtain the total absorption for the vibrational band (summed over the intensities of all rotational lines) from absorption measurements for a limited number of rotational lines in the spectrum. Such calculations can be performed for any known temperature using accurate spectral simulation programs such as the PGOPHER program employed here,[28] but absorption measurements through the arc jet plume sample radicals in regions that have a wide range of temperatures that change rapidly with location in the plume. This same problem was recognized by Lombardi *et al.*[29] when comparing diode laser absorption measurements with model outputs for a H_2/CH_4 microwave plasma. Two strategies can be adopted for the purposes of our data analysis. The first is to use an average temperature of the radicals of interest along the line of sight of the measurement. Previous studies of the $C_2(a)$ radical have established this average temperature to be 3300 ± 200 K along a line through the center of the plume (i.e., at height $x=0$) by Boltzmann analysis of absorption spectra spanning large swathes of the vibrationally diagonal $d\,^3\Pi_g$-$a\,^3\Pi_u$ Swan band transitions.[19,21] The 3300 K mean temperature is unlikely to be valid for measurements made at $x\neq0$, however, and the temperature variation along the laser path cannot be derived from our measurements. For analysis of data obtained with the laser positioned at $x\neq0$ (and, for consistency, for $x=0$ data), we therefore adopt a second strategy in which we calculate column densities for single rotational levels of $C_2(a)$ or CH(X) radicals, denoted henceforth by the labels $C_2(a,v=0,J)$, or CH($X,v=0,N$) (where J and N are quantum numbers that describe the rotational angular momentum of the radical; N is used for CH to indicate exclusion of the effects of noninteger electron spin). The calculation of these J- or N-specific column densities requires no knowledge of the plume temperature, and results can be compared directly to the outputs of the computer model (*vide infra*). In practice, the reported column densities will often be the result of an average over two or three rotational levels obtained because we scan small regions of the spectrum that cover a few ro-

tational lines, in which case the mean J or N value will be specified.

Adapting the analysis of spectral line intensities described in Ref. 17 and using standard connections between absorption coefficients and decay rate coefficients for CRDS measurements,[30] we can write the column density for $C_2(a,v=0,J)$ radicals as

$$\{C_2(a,v=0,J)\} = \frac{8\pi L\bar{\nu}^2}{A_{00}}\int_{\text{line}}\Delta k\,d\bar{\nu}$$

$$= \sum_{i=1}^{n}\delta_i[C_2(a)]_i\,p_{v=0}(T_i)p(T_i). \quad (1)$$

Here, $\{Y\}$ denotes a column density of species Y. The terms in the central part of the equation relate to the experimental measurement and are defined as follows: L is the length of the ring-down cavity (100 cm); A_{00} is the Einstein A coefficient for the $v'=0$-$v''=0$ vibrational band of the $C_2\,d\,^3\Pi_g$-$a\,^3\Pi_u$ transition [$A_{00}=(7.21\pm0.30)\times10^6$ s^{-1} (Ref. 17)]; $\bar{\nu}$ is the wavenumber of the spectral line (in cm^{-1}); Δk is the wavenumber-dependent change in the ring-down decay rate coefficient as a result of C_2 absorption, and is integrated across the full width of the rotational spectral line. The terms on the right-hand side of Eq. (1) relate to the computer model: the index i labels each of the n cells of length δ_i along the path of the laser beam (in the y direction, at fixed x and z); $[C_2(a)]_i$ is the number density of $C_2(a)$ radicals in a particular cell, T_i is the gas temperature in the ith cell; $p_{v=0}(T_i)$ is a vibrational partition function, and $p(T_i)$ is a rotational level weighting factor calculated from the PGOPHER spectral simulation program.[28] This factor is the calculated ratio of the integrated intensity of the single, rotationally resolved spectral line being studied to the intensity of the full vibrational band (evaluated as the sum of the integrated intensities of every rotational feature) at the temperature T_i of the ith cell. Multiplication of $[C_2(a)]_i$ by $p_{v=0}(T_i)\cdot p(T_i)$ thus gives the number density of $C_2(a)$ radicals in their $v=0$ vibrational level and a particular rotational level. An equivalent formula applies to the analysis of CH($X,v=0,N$) data [with $A_{00}=(1.85\pm0.05)\times10^6$ s^{-1} (Ref. 17)]. Equation (1) thus allows a quantitative and direct comparison of experimental measurements with model outputs with due allowance for the steep variations in temperature in the arc jet plume.

A. H($n=2$) column and radially dependent number densities

In previous publications, we reported measurements of the column densities and radial distributions of H($n=2$) atoms in the arc jet plume for flow of an Ar/H_2 gas feedstock mixture, with no added CH_4.[22,23] Data were obtained by CRDS using the Balmer-β absorption line at 486.1 nm and diode laser absorption via the Balmer-α transition at 656.3 nm, and analysis of Stark broadened line shapes provided information on changes in the electron density in the plume as the flow of H_2 was varied. Column densities of H($n=2$) for various H_2 flow rates were in good agreement at $z=140$ mm for the two spectroscopic methods and decreased

with increasing H_2 flow above 0.5 SLM. Here, we extend these prior measurements to include the effects of added CH_4 on the $H(n=2)$ atom and electron number densities. We concentrate on $H(n=2)$ atoms rather than ground electronic state $H(n=1)$ atoms for a variety of reasons. Quantitative detection of ground state H atoms by direct absorption requires vacuum ultraviolet (VUV) radiation at wavelengths of 121.6 nm or less and presents problems not only in stable generation of the radiation but also in the use of transmissive optics. Moreover, the plasma is optically thick at these wavelengths because of the very high density of $H(n=1)$ atoms, thus complicating reliable retrieval by absorption methods. Two-photon laser-induced fluorescence spectroscopy techniques[31–33] can be employed to avoid use of VUV wavelengths in the detection of $H(n=1)$ atoms, but very careful calibration is required to convert from relative to absolute number densities that are so important for critical evaluation of the model. $H(n \geq 2)$ atoms are formed in large part by recombination of an electron with ArH^+ (and perhaps also some $C_xH_y^+$) ions, and their number densities remain high because of reabsorption of radiation emitted as they decay to the $n=1$ quantum state. They thus serve as an important indicator of the local ion and electron chemistry within the arc jet plume.

At low H_2 flows (0.2 and 0.5 SLM) and in the absence of added CH_4, the $H(n=2)$ atoms measured at $z=140$ mm from the nozzle (and with the substrate at $z=168$ mm) were previously determined to be distributed with a maximum number density that peaks away from the core of the plume ($r>0$). For $F_{H_2}=0.2$ SLM, the maximum in the radial distribution occurred at $r=4$ mm, and for $F_{H_2}=0.5$ SLM, the maximum shifted inwards to $r \sim 2$ mm.[23] At higher H_2 flows, the $H(n=2)$ density measured at $z=140$ mm was seen to peak at $r=0$ and to decline steadily in magnitude because of more rapid depletion at shorter z of the Ar^+ ions that react with H_2 to make ArH^+ ions. The plume changes structure from a cylindrical shell of bright H-atom emission along its entire length, developing a characteristic luminous conical tip and retracting toward smaller z as $H(n \geq 2)$ number densities decline with increasing H_2 flow, and their distributions shift toward the plume axis. The $H(n=2)$ absorption lines (measured at $z=140$ mm) also sharpen as the H_2 flow is increased because the local electron density decreases and thus Stark-broadening effects of the electric field in the plasma are reduced.

With the behavior of $H(n=2)$ established for the base Ar/H_2 plasma, the consequences of added methane are now explored. Conversion of $H(n=2)$ absorption measurements into column densities requires a value for the Einstein A coefficient for the $H(n=3$ or $4 \leftarrow n=2)$ electronic transition that is integrated over all the fine-structure components, with the assumption that all spin-orbit components arising from $2s^1$ and $2p^1$ electronic configurations are statistically populated according to their orbital degeneracies.[22,23] Data for Einstein A coefficients for all fine-structure components of Balmer-α and β transitions were taken from the NIST database.[34] The $H(n=2)$ column density measured at $z=140$ mm is largely invariant with methane (0–80 SCCM) added to the plasma through the injection ring at a constant

H_2 flow rate of 500 SCCM. There is at most only a very weak decline in the $H(n=2)$ column density as the flow of methane increases. The column density data from both Balmer-α and Balmer-β transition measurements are in quantitative agreement, with mean values of $(5.4 \pm 0.7) \times 10^{11}$ and $(5.6 \pm 0.6) \times 10^{11}$ cm^{-2}, respectively, for the 0–80 SCCM range of methane flows. The values obtained at $F_{CH_4}=0$ SCCM are also in excellent accord with our previous measurements.[22,23] The model calculations show some variation with added CH_4: the column densities of $H(n=2)$ are 7.9×10^{11} cm^{-2} for $F_{CH_4}=0$ SCCM and 1.3×10^{12} cm^{-2} for $F_{CH_4}=80$ SCCM (at 500 SCCM H_2). The electron density, derived from the Stark broadening of the Balmer-β line, is a very weakly increasing function of methane flow rate: initial addition of methane causes a slight rise in the measured electron density, but the values of $(2.9 \pm 0.6) \times 10^{14}$ cm^{-3} are essentially independent of the methane flow rate over the range of flows $F_{CH_4}=10$–60 SCCM and $F_{H_2}=500$ SCCM. The agreement between the measurements reported here for $F_{CH_4}=0$ SCCM and $F_{H_2}=500$ SCCM and those obtained previously for the arc jet operating on an Ar/H_2 feedstock is excellent,[22] and model and measured electron number densities for $F_{CH_4}=0$ and 80 SCCM are in satisfactory accord. Methane addition is seen to have only a minor influence on determining the electron density at a distance $z=140$ mm from the N-torch nozzle.

Radial profiles of the $H(n=2)$ number density, obtained by Abel inversion of x-dependent Balmer-α diode laser absorption column density measurements, for $F_{H_2}=500$ SCCM and a range of CH_4 flow rates are shown in Fig. 2. The error bars plotted in the data derive from uncertainties in the spatially dependent column densities obtained from the experimental measurements. Abel inversion of each half of the measured column density profiles provides a separate determination of the r-dependent number densities, and the differences between the two outcomes determine the error bars, with plotted points representing the mean values of the derived number densities at each r. The measured densities of atomic $H(n=2)$ are largely invariant with increasing methane flow rate. Peak values of the number densities occur at $r=2$ mm and lie in the range of $(5-8) \times 10^{11}$ cm^{-3}. The measured radial distributions extend out to 6 mm from the center of the plume. In comparison, a previously published radial profile of $H(n=2)$ number densities, obtained under the same conditions of Ar and H_2 inlet flows, and in the absence of added CH_4, also peaked at $r=2$ mm, extended to 6 mm, and showed an $H(n=2)$ number density at the peak of the radial profile of 9×10^{11} cm^{-3}, confirming the reproducibility of our measurements. The radial profiles dip at $r=0$ mm, as a result of the formation mechanism of $H(n=2)$ atoms which involves reaction of Ar^+ ions with H_2 followed by dissociative electron attachment to ArH^+. This mechanism favors formation of ArH^+ ions at the boundary of the plume because of the need for radial diffusion of H_2 into the activated gas plume. The equivalent data derived from the model (plotted in Fig. 4 of the accompanying paper[24]) are in
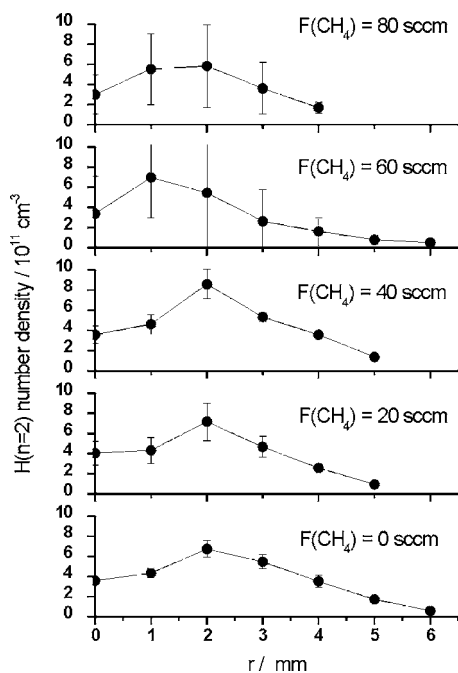
FIG. 2. Experimentally derived H($n=2$) number densities as a function of radial distance from the plume center for CH_4 flows from 0 SCCM (bottom) to 80 SCCM (top). The input flow of H_2 was 500 SCCM, with a total input gas flow of 13.2 SLM and the arc jet operating power was 6.4 kW. The error bars encompass the difference in outcomes of analysis of data obtained at each pair of $+x$ and $-x$ displacements, with the average value plotted. The results for $F(CH_4)=0$ and 80 SCCM can be compared directly with the results of the model calculations plotted in Fig. 4 of the accompanying paper (Ref. 24).

good agreement with the measured radial dependencies of H($n=2$) number densities, although the peak densities are overestimated.

B. Temperatures and column densities of $C_2(a)$, $C_2(X)$, and CH(X) radicals

Column densities for $C_2(a\ ^3\Pi_u)$, $C_2(X\ ^1\Sigma_g^+)$, and CH($X\ ^2\Pi$) radicals in selected rovibrational states were obtained using CRDS at respective wavelength regions of 515 nm (C_2 Swan band, $d\ ^3\Pi_g$-$a\ ^3\Pi_u$ $v'=0\leftarrow v''=0$), 231 nm (C_2 Mulliken band $D\ ^1\Sigma_u^+$-$X\ ^1\Sigma_g^+$, $v'=0\leftarrow v''=0$), and 426 nm (CH $A^2\Delta$-$X^2\Pi$, $v'=0\leftarrow v''=0$). Changes in the ring-down rate as the laser wavelength was scanned across an absorption line were converted to column densities as discussed at the start of Sec. III, using values for the Einstein A coefficients (or equivalently oscillator strengths) of the electronic transitions (as described in Refs. 17 and 20 for the Swan and Mulliken band measurements). For the reasons given earlier, we focus on intercomparison of experimental and model column density data for one, or a few, rotational levels of $v=0$. Figure 3 shows the portion of the C_2 spectrum selected for spatially resolved measurements of column densities described in Sec. III B 1. With predictions from the computer model of the spatial variation of distributions of temperature and radical number densities in the plume, experimental data can be compared with forward simulation of the predicted (from the model) line-of-sight column densities to check correspondence between the model outputs and the experimental measurements.
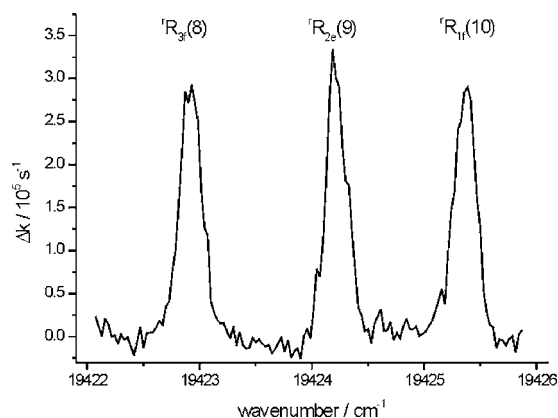

FIG. 3. A CRD spectrum of the portion of the $C_2\ d\ ^3\Pi_g$-$a\ ^3\Pi_u$ absorption band used for spatially resolved measurements of $C_2(a,v=0)$ column densities. The lines are assigned to rotationally resolved transitions using the labeling scheme $^{\Delta N}\Delta J_q(J'')$, where J'' is the total angular momentum quantum number in the $a\ ^3\Pi_u$ state and q denotes spin orbit and parity labels.

In the following sections, results are considered in turn from measurements of radical temperatures (by two spectroscopic methods), column densities at $x=0$ for $C_2(X,v=0,J)$, $C_2(a,v=0,J)$, and CH($X,v=0,N$), and spatially resolved $C_2(a,v=0,J)$ and CH($X,v=0,N$) column densities at a range of values of x that span the plume. The results are discussed within the context of comparisons with the predictions of the model. Experimental measurements of $C_2(a,v=0)$ span rotational lines originating from levels with $J=8-10$; where averages are taken over absorption measurements for these lines, $\bar{J}=9$ is specified. For CH($X,v=0$) spectral data, $\bar{N}=7$.

1. Temperature measurements

The temperatures of electrons and heavy particles depend strongly on location in the plume, but fast energy exchange should ensure equilibration of translational, rotational, and vibrational temperatures of neutral and charged species at any particular point. A single temperature cannot, however, be used to describe the C_2 or CH radicals probed by CRDS because the measurement averages over their spatial distributions. The experiment will instead obtain mean temperatures of the radicals, averaged along a line of sight, and weighted by the nonuniform spatial distribution of number densities. Two methods to derive such mean temperatures are Boltzmann analysis of intensities of rotationally resolved features or fitting of rotational line profiles to Gaussian line shapes, with deconvolution of the effects of the laser bandwidth from those of Doppler broadening. The resultant Doppler broadened width is proportional to the square root of the translational temperature of the gas. Previous analysis of $C_2(d$-$a)$ spectra by both methods gave temperatures in the free plume of 3300 ± 200 K. As noted above, there is inevitably some averaging in these values because the plume is not homogeneous either in temperature or in the spatial distributions of the radicals, but the values reflect the temperatures in the regions of the plume where the radical number densities maximize. Spectra of CH obtained in the restricted wavenumber range of 23 415–23 435 cm^{-1} provide an esti-

mate of the mean temperature of $\leqslant 4000$ K: spectral lines originating from high rotational levels ($N=27$ and above), that simulations demonstrate to be of measurable intensity at temperatures >4000 K, are not seen above the noise levels of our data. The model calculations return temperatures for $C_2(a)$ and CH of $T_{calc}(C_2)=3870$ K and $T_{calc}(CH)=4300-4670$ K averaged along a plausible column length, with appropriate weighting for the radical number density distribution. A detailed temperature map is presented in the accompanying paper. Species at larger r have a lower temperature than those nearer the plume core, so the gas temperature estimated from spectra obtained as line-of-sight averaged measurements is likely be lower than the maximum values predicted by the model. As will be demonstrated experimentally and from model calculations, the C_2 radicals exhibit an off-axis peak in local number density, therefore the local gas temperature probed by spectroscopic measurements of $C_2(a)$ is not the maximum gas temperature of the plume and is lower than that for CH. Small discrepancies in the r-dependent number density profiles from the model might account for observed differences in calculated and experimentally derived temperatures for C_2 and CH.

Analysis of the translational temperature measured in the Ar/H$_2$/CH$_4$ plasma under standard growth conditions was performed previously on the arc jet plume as a function of distance from the substrate.[20] The constraints of the reactor design mean that the z location of the laser cannot be moved significantly; boundary effects near the substrate have therefore been investigated by moving the substrate toward the fixed nozzle and laser position. The apparent translational temperature derived from the Doppler broadening of a C_2 Swan band rotational line was found to increase on approaching the substrate:[17] at 1 mm from the substrate, the measured Doppler broadening led to temperature estimates as high as 4800 ± 400 K. The rotational temperature can be derived from spectra recorded over a much larger wavenumber range than was used for the column density measurements (to ensure a wide range of rotational energies of the C_2 are sampled). Rotational temperatures are derived from the line intensities, and thus level populations, assuming a Boltzmann distribution. Such Boltzmann plots can be curved because $C_2(a)$ radicals in lower J levels are more likely to be found in cooler regions of the plume, whereas higher J levels are populated preferentially by $C_2(a)$ radicals in hotter regions. Accurate energies of the rotational levels of $C_2(a)$ were calculated from available spectroscopic constants using the PGOPHER simulation program.[28] The rotational temperature was found to remain at ~3200 K over the range of $2-25$ mm from the substrate. The two apparently conflicting temperature measurement outcomes are reconciled by recognizing that the Doppler broadening measurements in proximity to the substrate are affected not only by the local temperature but also by the flaring of the plume as it strikes the substrate. This plume flaring increases the components of the velocity of the plume along the laser propagation axis, an effect that can be simulated using the velocity fields from the model, and the temperature derived from the Boltzmann analysis.[20,35]

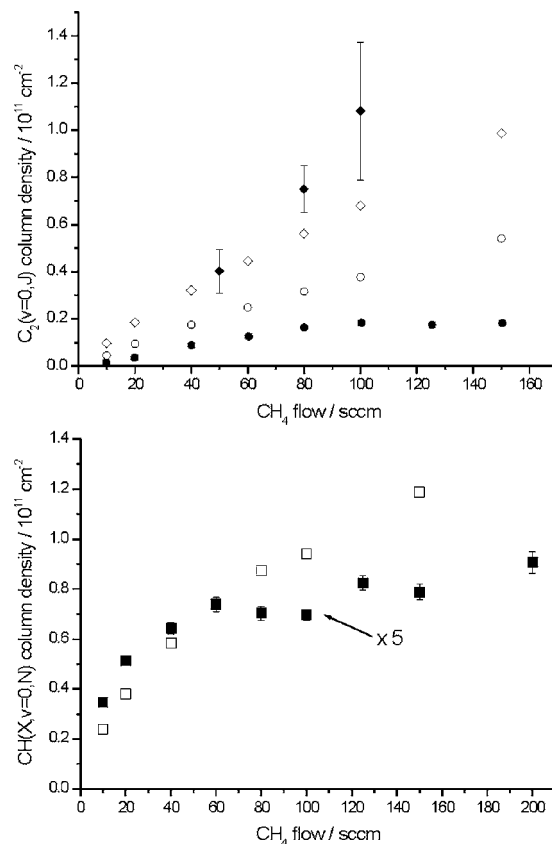

FIG. 4. Experimentally measured (black symbols) and model calculated (white symbols) $C_2(a,v=0,\bar{J}=9)$ (● and ○) and $C_2(X,v=0,\bar{J}=14)$ (◆ and ◇) (top panel) and CH($X,v=0,\bar{N}=7$) (■ and □) (bottom panel) column densities obtained at a height $x=0$ through the plume and for various methane flow rates. The arc jet was operated under otherwise standard conditions as defined in the text. For C_2 measurements the input power was 6.4 kW and for CH data it was 6.8 kW. The experimentally measured CH column densities have been multiplied by 5 for display purposes. The error bars on experimental data are $\pm 1\sigma$ for repeat measurements and may be smaller than the plotted symbols.

2. $C_2(a)$, $C_2(X)$, and CH(X) column densities

Figure 4 illustrates the $C_2(a,v=0,J)$, $C_2(X,v=0,J)$, and CH($X,v=0,N$) column densities measured at $x=0$ mm with flows of added CH$_4$ in the range of $0-200$ SCCM, under otherwise standard operating conditions, as defined in Sec. II. The previously reported experimental measurements for $C_2(a)$ and $C_2(X)$ (Refs. 17 and 20) and current data for CH(X) are compared with the predictions of the model, which captures the trends of increasing C_2 column densities up to a methane flow of 100 SCCM. Experimental measurements of $C_2(a,v=0,J)$ then reveal a plateau region in which these radical densities no longer rise as more methane is added. A similar plateau is observed for CH($X,v=0,N$) column densities for methane flows from 40 to 150 SCCM. This behavior confirms earlier measurements of Wills *et al.*,[17] but the absolute values shown in Fig. 4 are approximately a factor of 2 lower than the CH($X,v=0,N$) column densities obtained in our earlier study. Such variations in absolute radical column densities have been observed previously for measurements made on the arc jet reactor at different times and are argued to be a consequence of degradation of the performance of the dc discharge with extended (a few
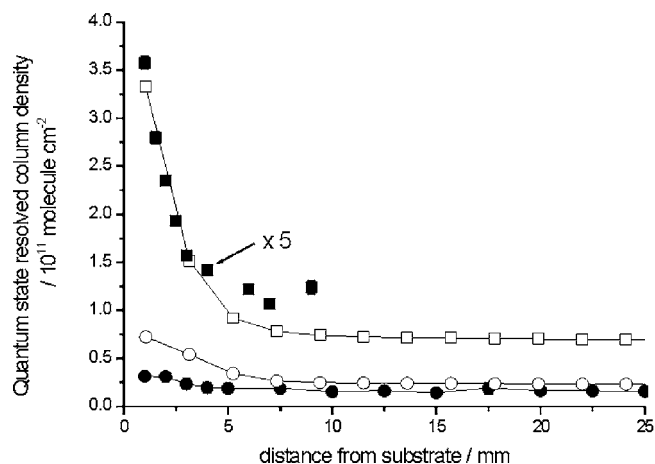
FIG. 5. Experimental (black symbols) and model (white symbols) column densities of $C_2(a, v=0, \bar{J}=9)$ (● and ○) and $CH(X, v=0, \bar{N}=7)$ (■ and □) as a function of distance from the substrate. The experimentally measured CH column densities have been multiplied by 5 for display purposes. The error bars on experimental data are $\pm 1\sigma$ for repeat measurements.

tens of hours) use of the reactor. As was noted by Rennick *et al.*,[20] the ratio of column densities of $C_2(a)$ and $C_2(X)$ at a fixed flow of CH_4 is close to that expected for a Boltzmann distribution at a temperature of ~ 3300 K, despite the expected greater reactivity of $C_2(X)$ radicals with species such as H_2.[36] This observation was interpreted as indicative of rapid replenishment of $C_2(X)$, depleted by chemical reaction, by collisional relaxation of $C_2(a)$. There is factor of ~ 5 discrepancy between the calculated and measured CH column densities, but the C_2 data agree to within a factor of 2 at methane flows up to 100 SCCM. The model does not, however, reproduce the experimentally observed plateaus in radical column densities for the higher methane flows; instead, it exhibits a trend of increasing C_2 and CH column densities for CH_4 flows up to 150 SCCM. Precise reasons for these differences have not been identified, but may arise from formation of higher hydrocarbon radicals and molecules in the cooler regions of the reactor or soot formation in the recirculation region where temperatures are optimum for such processes.[37] Higher hydrocarbons and soot provide sinks for carbon, for which the chemistry is not incorporated in the model mechanism.

The dependence of $CH(X, v=0, N)$ column densities on input power to the reactor was explored for powers in the range of 5.5–7.8 kW. Consistent with our previous study,[17] the CH column densities were observed to be invariant with discharge power. $C_2(a, v=0)$ column densities, however, show a weakly rising trend as the power is increased over this range.

Figure 5 shows the dependence of $C_2(a, v=0, J)$ and $CH(X, v=0, N)$ column densities on distance from the substrate, obtained from experimental measurements (with a fixed laser beam position and axial translation of the substrate) and computational data. The flaring of the plasma after impact with the substrate increases the length of the column of absorbing C_2 or CH and thus the column densities for distances less than 7 mm from the surface. Again, the absolute values of C_2 column density data agree well with

the model calculations, but factor of $\sim 3-5$ discrepancies persist for the CH data, with the model predicting higher column densities than are experimentally measured.

3. Spatial variation of $C_2(a)$ and $CH(X)$ column densities

Additional stringent tests of the computational model performance come from spatially resolved absorption data. The model predicts that the radial distribution of C_2, C_2H, C_3, C_3H, C_4, and C_4H radical number densities is annular, showing a depletion of density at the core of the plasma. Similarly localized depletion of C_3 density has been measured by LIF in another, lower power arc jet reactor,[6] but C_2 was observed to peak near the core of that plasma plume. In the current study, absorption lines in the C_2 Swan band were measured using the translatable cavity CRDS arrangement described in Sec. II, allowing the quantification of column density as a function of x, the distance from the plume centerline. At a distance $z=145$ mm from the nozzle, spectra were collected by CRDS over the wavenumber region from 19 422 to 19 426 cm^{-1} [covering the $^rR_{3f}(8)$, $^rR_{2e}(9)$, and $^rR_{1f}(10)$ lines shown in Fig. 3] and $CH(X)$ over the wavenumber interval of 23 422–23 428 cm^{-1} [spanning the $R_{1e}(7.5)$, $R_{2f}(6.5)$, $R_{1f}(7.5)$, and $R_{2e}(6.5)$ transitions with $N=6-8$] across the range of $-12 \leqslant x \leqslant 12$ mm at 1 mm spatial resolution. Initial data analysis involved Abel inversion to obtain radially dependent number density profiles, using a similar procedure to that described in Ref. 38 The raw data of column density as a function of x were symmetrized by folding about the center $(x=0)$ and smoothed by a three-point moving average to minimize the effect of noise on the inverted profiles. Such an analysis only gives an estimate of the number densities because of the effects of nonuniform temperature and thus varying $C_2(d-a)$ and $CH(A-X)$ absorption cross sections along the line of sight of the absorption measurements. Our preferred method of intercomparison of the experimental and model results is thus to use the data from the model to simulate the x-dependent column density measurements. These simulations were carried out in accord with Eq. (1) by summing the computed $C_2(a)$ and/or $CH(X)$ column densities in each cell of the model output; with due allowance for the calculated temperatures, these densities were converted to column densities for $C_2(a, v=0, \bar{J}=9)$ and $CH(X, v=0, \bar{N}=7)$ [evaluated using a vibrational partition function $p_{v=0}(T)$ and a rotational level weighting from the $p(T)$ factor for each cell, with the latter calculated using the PGOPHER simulations[19]]. Such forward simulations can be compared directly with experimental data measured as a function of H_2 flow rate (at fixed Ar and CH_4 flows) and as a function of CH_4 flow rate (with the H_2 and Ar flow rates fixed), and the outcomes are discussed in turn below.

The effect of varying the flow rates of H_2 and CH_4 supplied to the plasma was investigated under otherwise standard conditions of 6.4 kW input power and $F_{Ar}=13.2$ SLM at $z=145$ mm from the nozzle, with the experimental and model results compared in Figs. 6–9. Measured $C_2(a, v=0, \bar{J}=9)$ and $CH(X, v=0, \bar{N}=7)$ column densities (for rovibrational quantum states, as discussed earlier) as a function
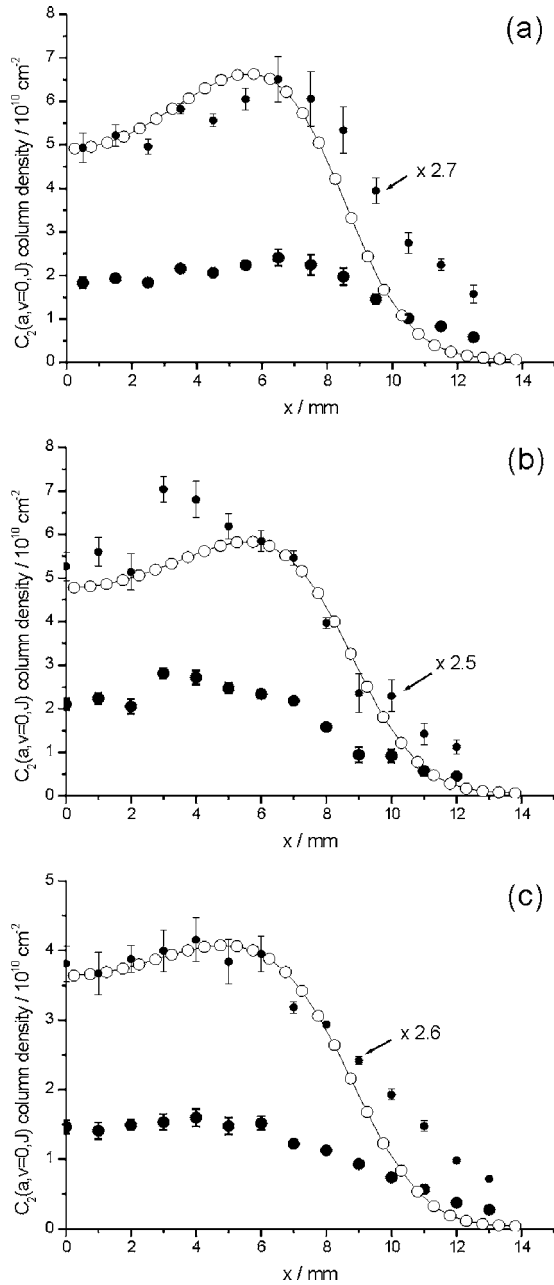
FIG. 6. Experimental measurements (large ●) and model predictions (○) of the *x*-dependent column densities of $C_2(a, v=0, \bar{J}=9)$ as a function of H_2 flow, with the arc jet operating under otherwise standard conditions. Flows of H_2 are (a) 500, (b) 1000, and (c) 1500 SCCM. The error bars are estimated from the fits to C_2 absorption data and the asymmetry of the profiles about their centers, and in some cases are smaller than the plotted symbols. The measurements are an average over ±0.3 mm (the laser beam width) centered at the plotted *x* value. The experimental data and associated uncertainties have been vertically scaled (small ●) by a constant factor, specified in each panel, for clearer comparison of their *x* dependence with the calculated profiles.

FIG. 7. Experimental measurements (●) and model calculations (○) of the *x*-dependent column densities of $C_2(a, v=0, \bar{J}=9)$ as a function of CH_4 flow, with the arc jet operating under otherwise standard conditions. The flow rate of H_2 is 1800 SCCM. Methane flow rates are (a) 20 SCCM, (b) 40 SCCM, and (c) 80 SCCM. The error bars are derived in the same way as for Fig. 6. The measurements are an average over ±0.3 mm (the laser beam width) centered at the plotted *x* value. The experimental data and associated uncertainties have been vertically scaled (small ●) by a constant factor for comparison of their *x* dependence with the calculated profiles.

of *x* position across the plasma for fixed $F_{CH_4} = 80$ SCCM are shown in Figs. 6 (H_2 flow rates of 500, 1000, and 1500 SCCM) and 8 (H_2 flow rates of 1000 and 1500 SCCM), respectively, together with predictions of the model. Further spectra were recorded and processed to determine the effect of added methane on the structure of the $C_2(a)$ and $CH(X)$ density distributions within the plasma plume. The *x*-dependent $C_2(a, v=0, \bar{J}=9)$ and $CH(X, v$
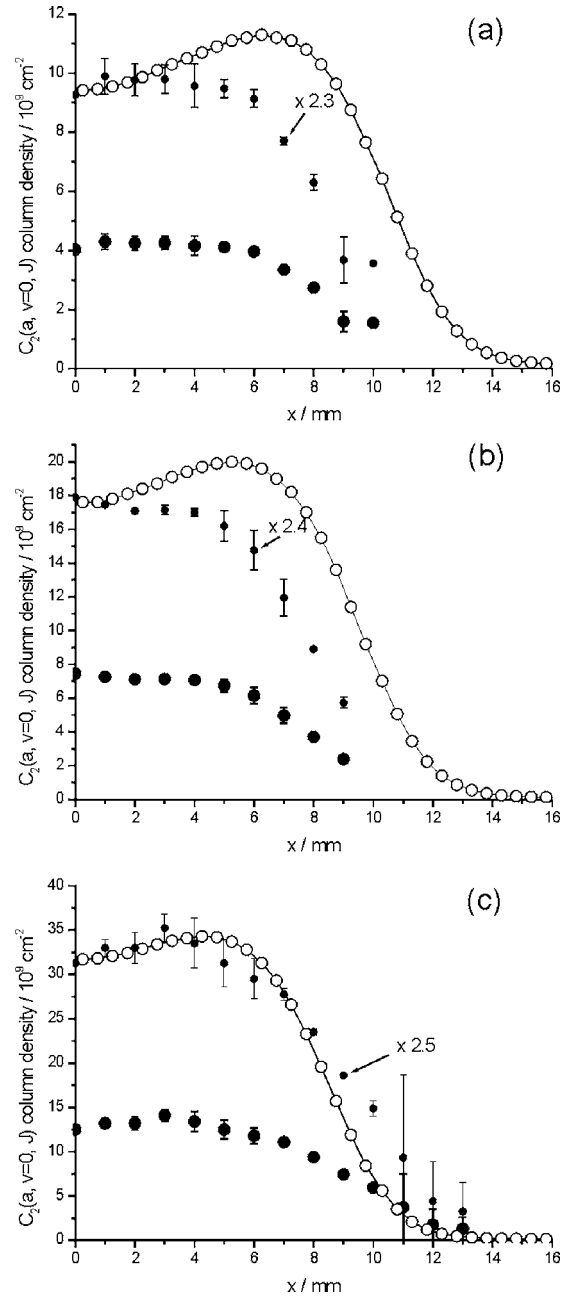
$=0, \bar{N}=7)$ column densities for several input CH_4 flow rates, at constant $F_{H_2} = 1800$ SCCM, are shown in Figs. 7 and 9, respectively, and compared with the simulated column densities from the model.

For clarity of comparison of the calculated and measured, *x*-dependent column density profiles, the experimental data have also been vertically scaled by factors determined by eye for each data set in the figures. Some discrepancies are evident between the computed and measured profiles. For
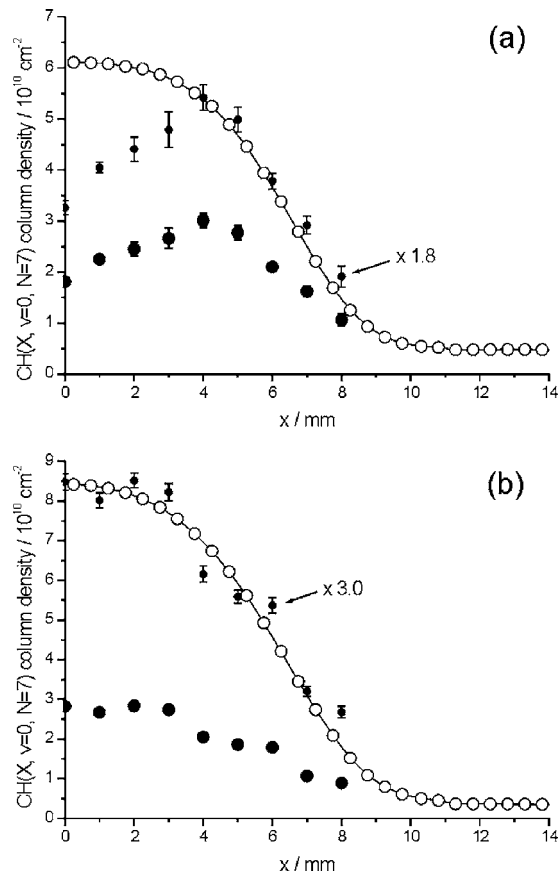
FIG. 8. Experimental (●) and model calculated (○) x-dependent column densities of CH(X,v=0,N) radicals for two flows of H₂ with the arc jet operating under otherwise standard conditions. Flows of H₂ are (a) 1000 and (b) 1500 SCCM. The error bars are estimated from the fits to CH absorption data and the asymmetry of the profiles about their centers, and in some cases are smaller than the plotted symbols. The measurements are an average over ±0.3 mm (the laser beam width) centered at the plotted x value. The experimental data and associated uncertainties have been vertically scaled (small ●) by a constant factor for comparison of their x dependence with the calculated profiles.

example, the width of the profile in Fig. 6(a) is underestimated by ∼1 mm by the model; in Fig. 6(b), there is some scatter in the experimental data at $x = 3-4$ mm that may have been a consequence of plume instabilities. The experimental C₂ column density profiles for different CH₄ flow rates at $F_{H_2} = 1800$ SCCM, plotted in Figs. 7(a) and 7(b), are clearly narrower than the model predicts, yet the agreement in Fig. 7(c) is good. In Fig. 8(a), the outer part of the CH column density profile is well matched by the model, but a dip evident in the experimental data at small x is not reproduced; in Fig. 8(b), however, the agreement between the measured and computed profiles is excellent. Over the duration of the measurements of such C₂ and CH profiles short-term fluctuations in the plume, and slower drift in the operating performance make reliable data difficult to accumulate and may account for some of these discrepancies. At the high H₂ flow rates used for the data in Fig. 7, the modeled radial dependences of the number densities of radicals, atoms, and electrons are very sensitive functions of distance from the nozzle;[22,23] the plume develops a conical tip, visible to the eye, at distances z corresponding to intersection of the plume with the laser

axis. Better matching of experimental and computed profiles at fixed z under these conditions is thus a considerable challenge.

The dips at $x=0$ for the experimental and model column density data displayed in Fig. 6 are a signature of annular structure in the $C_2(a, v=0, \bar{J}=9)$ number densities, with depletion of C₂ at the core of the plume at $z=145$ mm. Although the higher temperature at the plume center reduces the gas density, and thus concentration, the model calculations demonstrate that the principal cause of the dips is reduction in the C₂ mole fraction at small r (see Fig. 2 of the companion paper, Ref. 24). The depletion is more pronounced in number density than column density plots because column densities at small x sample both the core and the outer regions of the plume along the line of sight. The absolute values of the column densities do not change monotonically with H₂ flow rates. Calculations show that the main source of C₂ molecules is the reaction

$$C_2H + H \leftrightarrow C_2(X) + H_2, \tag{2}$$

with fast interconversion in collisions with different partners M,

$$C_2(X) + M \leftrightarrow C_2(a) + M. \tag{3}$$

The production sources are similar for all H₂ flow rates, but the dominant loss mechanisms in this plume region differ: for $F_{H_2} = 0.5$ SLM, it is the charge transfer reaction of C₂ molecules with Ar⁺ ions (the condition $[H_2] \ll [Ar^+]$, discussed in the accompanying paper, is realized in this case); whereas for $F_{H_2} = 1$ and 1.5 SLM, with more abundant H₂, it is the reverse H-shifting reaction (−2). Similar trends are observed in the CH production/loss rates, determined mainly by the H-shifting reaction,

$$CH + H \leftrightarrow C + H_2. \tag{4}$$

Some contributions to the CH loss are also provided by the charge transfer reaction,

$$Ar^+ + CH \leftrightarrow CH^+ + Ar. \tag{5}$$

The role of plasma chemistry is not so important for CH because there are no plume regions where the condition $[H] \ll [Ar^+]$ arises, unlike the condition $[H_2] \ll [Ar^+]$ mentioned for C₂. Regardless of H₂ flow rate, the reaction

$$H + C_2(X) \leftrightarrow C + CH \tag{6}$$

never becomes a dominant loss reaction for C₂ species. As the flow of H₂ increases, so the measured column densities maximize closer to $x=0$ (Fig. 8), which is indicative of a number density distribution for the cylindrically symmetric plume that peaks closer to $r=0$. Similar, but more pronounced behavior was observed for the spatial distributions of H(n=2) number densities in the base Ar/H₂ plasma measured at $z=140$ mm and accounted for by the depletion of Ar⁺ ions earlier in the core of the expanding plume as the flow of H₂ increases.[22]

The effect of increasing F_{CH_4} at fixed $F_{H_2} = 1800$ SCCM is different: the experimental data plotted in Fig. 7 suggest that the spatial distribution of $C_2(a, v=0, \bar{J}$
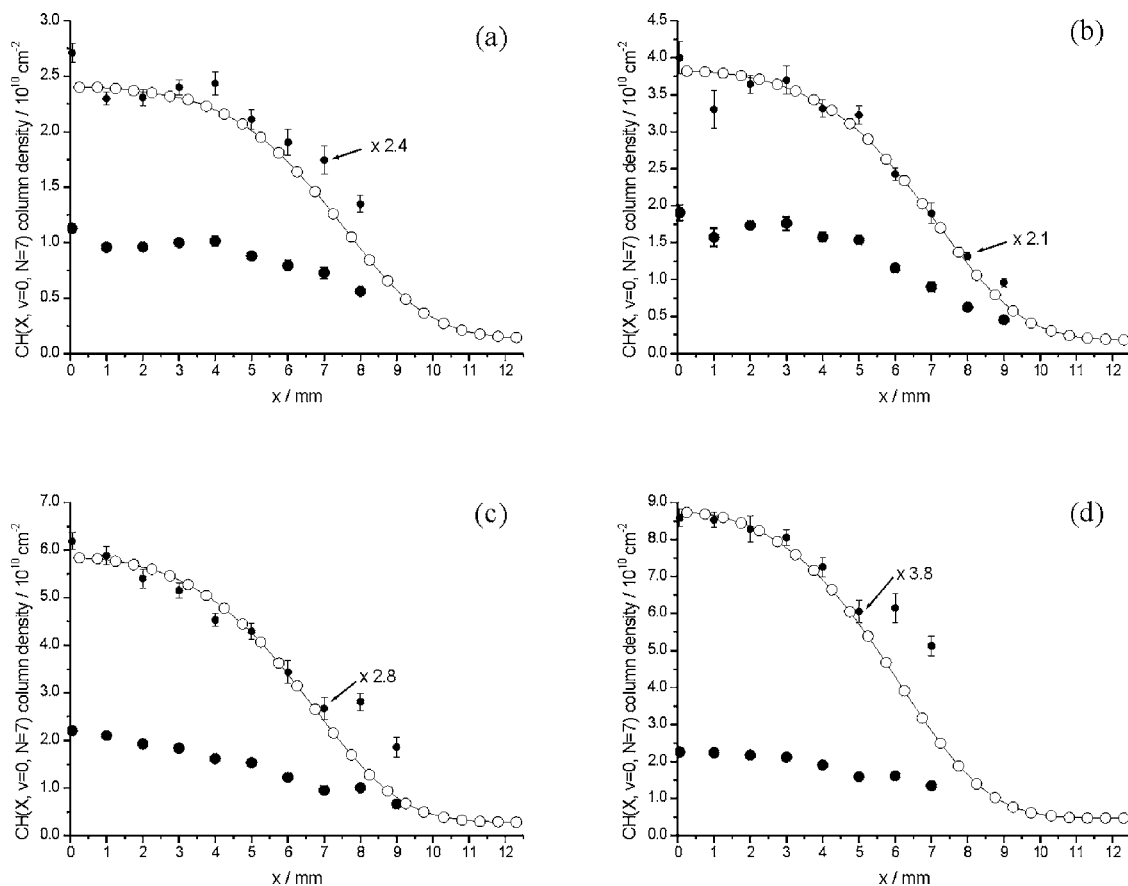
FIG. 9. Experimental measurements (●) and model calculations (○) of the x-dependent column densities of $CH(X, v=0, \bar{N}=7)$ as a function of CH_4 flow, with the arc jet operating under otherwise standard conditions. The flow rate of H_2 is 1800 SCCM. Methane flow rates are (a) 10 SCCM, (b) 20 SCCM, (c) 40 SCCM, and (d) 80 SCCM. The error bars are estimated in the same way as for Fig. 8. The measurements are an average over ±0.3 mm (the laser beam width) centered at the plotted x value. The experimental data and associated uncertainties have been vertically scaled (small ●) by a constant factor for comparison of their x dependence with the calculated profiles.

=9) radicals within the plume changes little, whereas the column density rises markedly. The increased methane flow rate will increase the concentration of hydrocarbon species in the off-plume regions of the chamber, thus increasing the fluxes of carbon-containing species diffusing into the plasma and enhancing C_2 densities. A similar effect of added CH_4 is observed for the spatially resolved column densities of $CH(X, v=0, \bar{N}=7)$ plotted in Fig. 9, although, as with the $x=0$ data shown in Fig. 4, the CH densities saturate for $F_{CH_4} \geqslant 40$ SCCM. The x-dependent column densities do not show a dramatic change in form with increasing methane flow, but the peak radical densities appear to shift toward the plume axis. Also noteworthy from comparison of Figs. 6–9 is that the spatial extents of the $C_2(a)$ and $CH(X)$ radicals in the plume are qualitatively similar, with C_2 extending slightly further out.

In addition to complex transport processes, the variable (r, z) distributions of the gas temperature and concentrations of H atoms, H_2, and primary ions all have a role in determining the observed dependence of CH, C_2, and other hydrocarbon species concentration profiles on the process parameters. The model captures the main trends, location, and radial profiles of the $C_2(a)$ and CH column density measurements, but overestimates the absolute values of the column densities. One possible reason for this overestimation and for the mod-

el's failure to reproduce the observed saturation of $C_2(a)$ and CH column densities with increasing CH_4 flow rate (Fig. 4) could be the omission (in the model) of reactions leading to heavy hydrocarbons in cooler regions of the reactor and to soot formation on remote surfaces of the reactor.

The boundary layer above the substrate in the arc jet reactor has not been considered in any of the preceding sections, but the effects of this very thin (<1 mm for our conditions), non-equilibrium layer are discussed in the companion paper.[24] For reasons given in Ref. 24, the boundary layer is not expected to alter significantly the chemical composition of the plume incident on the substrate surface. Experimental measurements of the chemistry within this narrow region are limited by scattering losses of the laser beam from the substrate surface and by the spatial resolution of the intracavity laser beam (with a beam waist of ~0.3 mm), so were not attempted.

IV. CONCLUSIONS

CRDS absorption measurements of column densities with x-direction spatial resolution are reported for $H(n=2)$ atoms and $C_2(a)$ and $CH(X)$ radicals, the latter with vibrational ($v=0$) and rotational quantum state resolution. The absolute column densities are derived without need for spec-

trometer calibration, and no assumptions other than cylindrical symmetry are required concerning the spatial inhomogeneity of number densities or temperature. The H($n=2$) measurements can be Abel inverted to obtain radially dependent number densities, but such a procedure is not possible for the diatomic radicals because their quantum state populations are temperature dependent. The number and column density data are compared directly with the outputs of a sophisticated computer model of the plasma reactor using forward simulation procedures and agree to within factors of 2–5 in almost all cases (with the model overestimating values of column and number densities). The model, which is described in the companion paper, captures the x, z, and r dependences of most of the reported experimental data and reveals considerable mechanistic information on the chemical processing in the arc jet plume.

ACKNOWLEDGMENTS

[1]*Thermal Properties and Applications of CVD Diamond, Low Pressure Synthetic Diamond: Manufacturing and Application*, edited by B. Dischler and C. Wild (Springer, Heidelberg, 1998).

[2]J. Gerbi, J. Vac. Sci. Technol. A (in press).

[3]P. W. May, Philos. Trans. R. Soc. London, Ser. A **358**, 473 (2000).

[4]J. Luque, W. Juchmann, and J. B. Jeffries, J. Appl. Phys. **82**, 2072 (1997).

[5]W. Juchmann, J. Luque, J. Wolfrum, and J. B. Jeffries, Diamond Relat. Mater. **7**, 165 (1998).

[6]W. Juchmann, J. Luque, and J. B. Jeffries, Appl. Opt. **39**, 3704 (2000).

[7]J. Benedikt, D. C. Schram, and M. C. M. van de Sanden, J. Phys. Chem. A **109**, 10153 (2005).

[8]P. Vankan, R. Engeln, and D. C. Schram, Appl. Phys. Lett. **86**, 101501 (2005).

[9]J. Benedikt, K. G. Y. Letourneur, M. Wisse, D. C. Schram, and M. C. M. van de Sanden, Diamond Relat. Mater. **11**, 989 (2002).

[10]M. G. H. Boogarts, S. Mazouffre, G. J. Brinkman, H. W. P. van der Heijden, P. Vanken, J. A. M. van der Mullen, D. C. Schram, and H. F. Dobele, Rev. Sci. Instrum. **73**, 73 (2002).

[11]M. F. A. M. van Hest, A. de Graaf, M. C. M. van de Sanden, and D. C. Schram, Plasma Sources Sci. Technol. **9**, 615 (2000).

[12]R. Engeln, K. G. Y. Letourneur, M. G. H. Boogarts, M. C. M. van de Sanden, and D. C. Schram, Chem. Phys. Lett. **310**, 405 (1999).

[13]M. C. M. van de Sanden, M. F. A. M. van Hest, A. de Graaf, A. H. M. Smets, K. G. Y. Letourneur, M. G. H. Boogarts, and D. C. Schram, Diamond Relat. Mater. **8**, 677 (1999).

[14]A. de Graaf, M. F. A. M. van Hest, M. C. M. van de Sanden, K. G. Y. Letourneur, and D. C. Schram, Appl. Phys. Lett. **74**, 2927 (1999).

[15]M. E. Coltrin and D. S. Dandy, J. Appl. Phys. **74**, 5803 (1993).

[16]B. W. Yu and S. L. Girshick, J. Appl. Phys. **75**, 3914 (1994).

[17]J. B. Wills, J. A. Smith, W. E. Boxford, J. M. F. Elks, M. N. R. Ashfold, and A. J. Orr-Ewing, J. Appl. Phys. **92**, 4213 (2002).

[18]Y. A. Mankelevich, N. V. Suetin, M. N. R. Ashfold, W. E. Boxford, A. J. Orr-Ewing, J. A. Smith, and J. B. Wills, Diamond Relat. Mater. **12**, 383 (2003).

[19]J. B. Wills, M. N. R. Ashfold, A. J. Orr-Ewing, Y. A. Mankelevich, and N. V. Suetin, Diamond Relat. Mater. **12**, 1346 (2003).

[20]C. J. Rennick, J. A. Smith, M. N. R. Ashfold, and A. J. Orr-Ewing, Chem. Phys. Lett. **383**, 518 (2004).

[21]C. J. Rennick, A. G. Smith, J. A. Smith, J. B. Wills, A. J. Orr-Ewing, M. N. R. Ashfold, Yu. A. Mankelevich, and N. V. Suetin, Diamond Relat. Mater. **13**, 561 (2004).

[22]C. J. Rennick, R. A. H. Engeln, J. A. Smith, A. J. Orr-Ewing, M. N. R. Ashfold, and Yu. A. Mankelevich, J. Appl. Phys. **97**, 113306 (2005).

[23]C. J. Rennick, J. Ma, M. N. R. Ashfold, A. J. Orr-Ewing, and Yu. A. Mankelevich, Plasma Sources Sci. Technol. **15**, 432 (2006).

[24]Yu. A. Mankelevich, M. N. R. Ashfold, and A. J. Orr-Ewing, J. Appl. Phys. **102**, 063310 (2007).

[25]A. E. Siegman, *Lasers* (Oxford University Press, Oxford, 1986).

[26]G. M. Lloyd and P. Ewart, J. Chem. Phys. **110**, 385 (1999).

[27]M. Zachwieja, J. Mol. Spectrosc. **170**, 285 (1995).

[28]C. M. Western, PGOPHER, a Program for Simulating Rotational Structure, University of Bristol, http://pgopher.chm.bris.ac.uk

[29]G. Lombardi, K. Hassouni, G. D. Stancu, L. Mechold, J. Röpcke, and A. Gicquel, Plasma Sources Sci. Technol. **14**, 440 (2005).

[30]M. D. Wheeler, S. M. Newman, A. J. Orr-Ewing, and M. N. R. Ashfold, J. Chem. Soc., Faraday Trans. **94**, 337 (1998).

[31]A. Gicquel, M. Chenevier, Y. Breton, M. Petiau, J. P. Booth, and K. Hassouni, J. Phys. III **6**, 1167 (1996).

[32]I. J. Wysong and J. A. Pobst, Appl. Phys. B: Lasers Opt. **67**, 193 (1998).

[33]W. Juchmann, J. Luque, and J. B. Jeffries, Appl. Opt. **44**, 6644 (2005).

[34]http://physics.nist.gov/PhysRefData/ASD/index.html

[35]C. J. Rennick, Ph.D. thesis, University of Bristol, 2006.

[36]M. Martin, J. Photochem. Photobiol., A **66**, 263 (1992).

[37]K. Hassouni, F. Mohasseb, F. Bénédic, G. Lombardi, and A. Gicquel, Pure Appl. Chem. **78**, 1127 (2006).

[38]Y. T. Cho and S. J. Na, Meas. Sci. Technol. **16**, 878 (2005).